Solar Phys
DOI 10.1007/s11207-015-0823-8

The *Hinode*/XRT Full-Sun Image Corrections and the Improved Synoptic Composite Image Archive

Aki Takeda[1] · Keiji Yoshimura[1] · Steven H. Saar[2]

Received: 30 March 2015 / Accepted: 23 November 2015

Abstract The XRT Synoptic Composite Image Archive (SCIA) is a storage and gallery of X-ray full-Sun images obtained through the synoptic program of the *X-Ray Telescope* (XRT) onboard the *Hinode* satellite. The archived images provide a quick history of solar activity through the daily and monthly layout pages and long-term data for morphological and quantitative studies of the X-ray corona. This article serves as an introduction to the SCIA, *i.e.*, to the structure of the archive and specification of the data products included therein. We also describe a number of techniques used to improve the quality of the archived images: preparation of composite images to increase intensity dynamic range, removal of dark spots that are due to contaminants on the CCD, and correction of the visible stray light contamination that has been detected on the Ti-poly and C-poly filter images since May 2012.

Keywords Corona · Data calibration · Instrumental effects · Instrumentation and data management

1. Introduction

The *X-Ray Telescope* (XRT) onboard the *Hinode* satellite is a grazing-incidence telescope, providing soft X-ray images of the Sun since October 2006 (Kosugi *et al.*, 2007; Golub *et al.*, 2007). Compared with its preceding telescope, the *Soft X-ray Telescope* (SXT) onboard *Yohkoh* (Ogawara *et al.*, 1991; Tsuneta *et al.*, 1991), XRT has higher angular resolution ($1'' \times 1''$) and higher sensitivity to the low-temperature plasma (≈ 1 MK). Since *Hinode* is a polar Sun-synchronous satellite, XRT is capable of continuous observation free from nights, except the period called "the eclipse season", when *Hinode*'s orbit crosses the shadow of the Earth in early May through mid-August.

✉ A. Takeda
takeda@solar.physics.montana.edu

1 Montana State University, P.O. Box 173840, Bozeman, MT 59717, USA

2 Smithsonian Astrophysical Observatory, 60 Garden Street, Cambridge, MA 02138, USA

Published online: 09 December 2015

Like most long-used instruments, XRT has problems with instrumental failures caused by aging or sometimes by unpredictable reasons. The examples relevant to this article are as follows.

1) Contamination on the CCD. A significant amount of contaminant accumulation was observed on the CCD surface during the initial phase of the mission. CCD bakeout operations were regularly performed every three weeks after February 2008. The source of the contaminants is likely to be a plasticizing agent used in the telescope tube or in the filter wheel assembly, but it has not yet been identified. The growth rate of the contaminants and their effects on the spectral and temperature response of the telescope was studied by Narukage *et al.* (2011). Their results are now included in the XRT standard analysis software for coronal temperature diagnostics (`XRT_TEEM`, *etc.*). Although most of the contaminants are removed by the regular CCD bakeout operations, a considerable number of small agglomeration of the contaminants ("droplets") are left unremoved on the CCD and observed as dark spots on the X-ray images. To these spots, which cover $\approx 5~\%$ of the full CCD area, correction can be applied for browsing purposes. We discuss the method in Section 3.

2) Reduced data rate. As a result of the anomaly of *Hinode*'s X-band antenna for data downlink, which occurred in January 2008, the onboard data volume allocated to XRT was reduced to ≈ 700 Mbits per typical day, which is several times lower than the value at the start of the mission. To accommodate this change, the data size, cadence, compression level, *etc.* are compromised as needed in the current operation.

3) Filter wheel glitch. XRT employs nine X-ray analysis filters and one visible-light (G-band) filter, held in two filter wheels (FW1 and FW2) mounted in series near the focal plane (Golub *et al.*, 2007; Narukage *et al.*, 2011). It turned out that one of the filter wheels (FW1) has a problem in rotation when operated at cool temperatures, typically encountered in the eclipse seasons. To avoid malfunction, the use of FW1 was withheld for the following periods, that is, most of 2010 and during the eclipse seasons after 2011. However, the long-term trend of the telescope status monitoring predicted that the FW1 temperature is warm enough for FW1 operation in recent eclipse seasons. In 2014, FW1 was operated during the eclipse season and caused no problem.

4) Visible stray-light contamination. Visible light contaminates the X-ray images taken with two of the nine X-ray filters since May 2012 because the pre-filter located at the entrance of the telescope failed. It is one of the purposes of this article to describe the currently applied method and the result of the stray-light correction (see Section 5).

Recent publications have described the new results of the XRT data calibration: Narukage *et al.* (2014) presented the recalibration of the thickness of the thick analysis filters and the resulting change in the XRT temperature response. Kobelski *et al.* (2014) discussed the uncertainties of the XRT data that arise from dark subtraction and JPEG data compression. Yoshimura and McKenzie (2015) introduced the co-alignment database improved by the analysis of *Hinode*'s Ultra Fine Sun Sensor(UFSS) output or by taking the cross-correlation with SDO/AIA images observed close in time.

The XRT synoptic program provides daily full-Sun images with a 34×34 arcmin field of view with a few selected filters (X-rays and G-band) since November 2006 to the present. The synoptic images were initially taken four times a day with a $1'' \times 1''$ resolution except for the period of CCD bakeout operation (and the period of XRT error and the following recovery operations). Since *Hinode*'s data rate was reduced in February 2008 (see item 2 above), they are obtained twice a day (around 6 and 18 UT) with a $2'' \times 2''$ resolution. The synoptic X-ray images processed for browsing (PNG format) are available to the public from the XRT Synoptic Composite Image Archive (SCIA) at http://solar.physics.montana.edu/hinode/xrt/. The synoptic images processed for analysis (FITS format) are archived as XRT official level 1 data and are accessible from the data search service at the Virtual Solar

Table 1 Statistical breakdown of the SCIA images as of 31 December 2014.

Total number of synoptic images	18 857
Open/Al-mesh filter images	5583
Open/Ti-poly filter images	6383
Open/Thick-Al filter images	33
Open/Thick-Be filter images	42
Al-poly/Open filter images	2996
C-poly/Open filter images	658
Thin-Be/Open filter images	2450
Med-Be/Open filter images	133
Med-Al/Open filter images	197
Al-poly/Al-mesh filter images	2
Al-poly/Ti-poly filter images	348
C-poly/Ti-poly filter images	32
Number of full-resolution images	6312
Number of half-resolution images	12 545

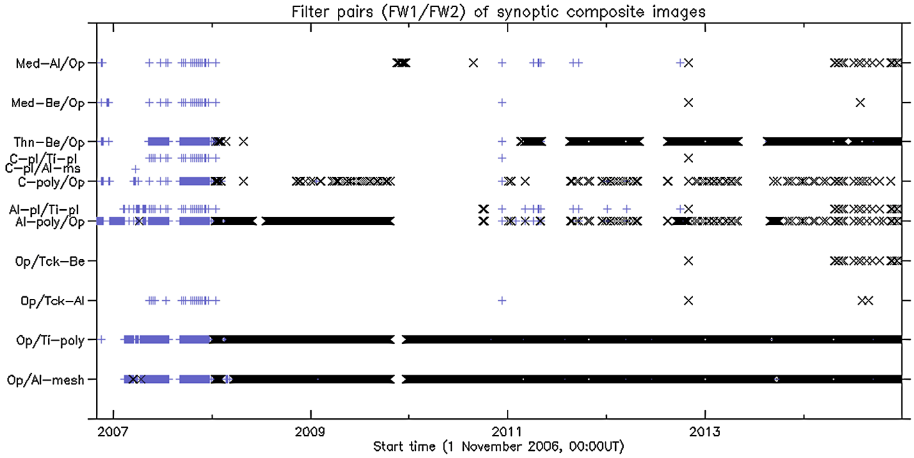

Figure 1 Temporal plot of the SCIA data availability by filter pairs and spatial resolution. The plus (+) signs (shown in blue) indicate the full-resolution (1″/pixel) images, while the cross (×) signs are images with half-resolution (2″/pixel).

Observatory (VSO; http://sdac.virtualsolar.org/cgi/search), or from the SCIA data site at http://solar.physics.montana.edu/Hinode/XRT/SCIA/synop_official. This paper introduces the SCIA and describes the method of processing applied to the archived images.

2. XRT Synoptic Composite Image Archive

The SCIA holds X-ray full-Sun images obtained through the XRT synoptic program. The total number of images exceeds 18 000 as of the end of 2014, as shown in Table 1. The temporal plot of their availability (Figure 1) indicates that the Al-mesh and Ti-poly filter

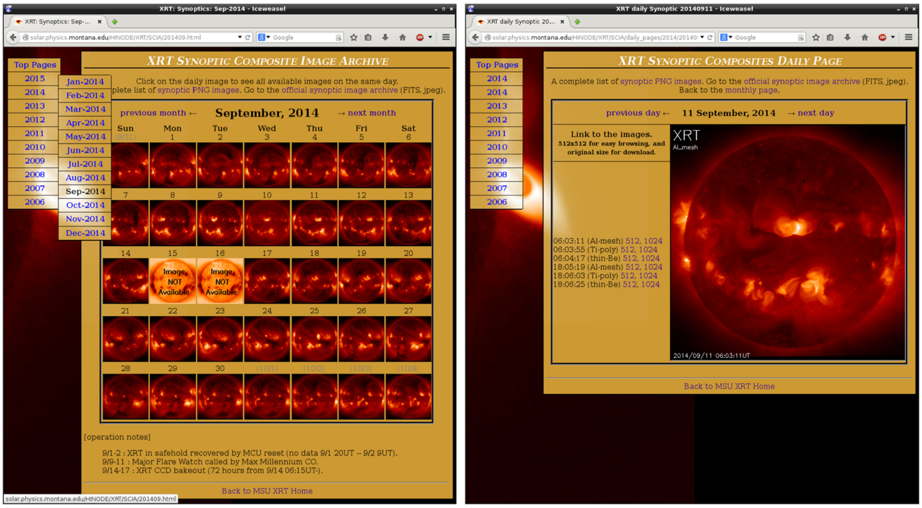

Figure 2 Example of SCIA web pages; monthly (left) and daily (right) pages.

images are most frequently and regularly taken through the entire mission. These thin filters provide high signal-to-noise ratio images over the solar activity cycle and enable us to diagnose temperatures of almost all coronal structures (1 to 10 MK) with the filter ratio method (Narukage *et al.*, 2011). The thin-Be filter was added to the regular sequence in 2010, and these images are obtained twice a day, the same frequency as the Al-mesh and Ti-poly filter images. The major periods of missing data are 26 July to 23 September 2007 for the investigation of CCD contamination, 7 to 23 February 2008 for the *Hinode* antenna problem, and 23 October to 19 December 2009 for the operational heater failure. The FW1 filters (Al-poly, C-poly, thin-Be, med-Be, and thick-Be) were not used during most of 2010 and the eclipse seasons (early-May to mid-August) of 2011 through 2013.

The SCIA has two layers of pages (Figure 2). Monthly pages consist of daily thumbnail images of the month, arranged similar to a monthly calendar. Daily pages work as a quick viewer of all the images available for the day. The pages on both layers are connected to each other with symbolic links, so that users can move back and forth between the layers.

All the images in SCIA are made from the XRT level-0 FITS data files (*i.e.*, official raw data before correction) and are processed either for analysis (FITS format) or for browsing (PNG format). For both analysis and browse images, the basic correction (dark subtraction, intensity normalization, *etc.*) were applied through the XRT standard analysis software (`XRT_PREP`) included in the SolarSoftWare (SSW; Freeland and Handy, 1998). Other corrections, which were initially performed separately but are now handled by the process with `XRT_PREP`, are the removal of the spots caused by the contamination on the CCD (see Section 1) and the improvement of the satellite pointing information. The technique used in the contamination spot removal is described in Section 3. The pointing information, which is crucial for co-aligning the images with those from instruments other than *Hinode*, are corrected by referring to the co-alignment database developed by Yoshimura and McKenzie (2015). The corrected information is passed in the FITS header of the images for analysis.

The composite image technique is applied to both analysis and browse images for the purpose of increasing the intensity dynamic range of the whole image. It is demonstrated in Section 4.

The visible stray-light contamination (see Section 1) is corrected by subtracting the stray-light pattern obtained during *Hinode*'s eclipse seasons. This correction is currently applied only to browse images. The quantitative analysis is sensitive to the amount of the stray-light intensity and requires careful evaluation case by case. Details are discussed in Section 5.

The same procedure except for the use of co-alignment database is applied to the XRT quick-look data files (*e.g.*, quickly prepared raw data used for satellite operations and data verification). They are used for checking the quality of the synoptic composites and for providing near real time full-Sun images to the public, but are not included in the SCIA.

3. Contamination Spot Correction

There are two main sources of localized, non-solar blemishes in the XRT data: dust and contamination spots. Both reduce the received X-ray count rates in small (typically < 100 pixel) regions and need to be mitigated to make cosmetically optimal images.

The dust features have been present from the start of the mission and consist of 159 generally small (average size 6.5 pixels, the largest is 134 pixels; each pixel is 13.5 μm or $1.0286''$ square) opaque (or nearly so) features. Although initially fixed in number and properties, the average dust size has varied periodically since the apparent entrance filter breach. The variation is seemingly in phase with the growth of the contamination layer between the CCD bakeouts. We discuss this further below.

Contamination spots appeared after the first CCD bakeout (23 July 2007), which was done to remove (from the CCD at least) the layer of unknown contaminant that had been building up on the CCD and filters. After bakeout, some of this contaminant collected into spots on the CCD. Empirically, the spots do not change in size or increase in number over time as long as the bakeouts are performed regularly. This fact was not appreciated immediately, so that when the second bakeout was conducted about six months after the first (29 January 2008), additional spots were added and spot sizes increased. Thereafter, regular (roughly monthly) bakeouts have been performed, and no significant change in spot number or size has been detected. Thus there are two epochs of spot formation; the first epoch left 2.6 % of the CCD covered by 12261 spots (average size 8.9 pixels, maximum size 135 pixels), and the second left 5.5 % covered by 14 063 spots (average size 16.4 pixels, maximum size 183 pixels).

Both of these blemish types must be corrected for to yield the most cosmetically pleasing image. Nodding the telescope a few arc-seconds and patching the spots or dust in one with the revealed areas in the second nodded exposure could in principle correct all but the more quickly evolving features, but in practice this is too disruptive of spacecraft operations. Attempts have also been made to remove the spots in a sort of flatfield correction. Unfortunately, a simple constant flatfield value for each spot fails since the spot absorption appears to be wavelength or energy dependent; the spots are less opaque to hotter features (*e.g.*, active regions). Attempts to determine the wavelength dependence of the spot-absorbing material as a function of spot parameters (or on an individual basis) have so far been unsatisfactory. We have thus chosen a simpler, though less rigorous, expedient and simply estimated the missing flux based on interpolation from pixels at the spot boundaries.

Spot and dust locations and coverage are determined from a set of four quadrant images wherein four short (44 – 66 ms) exposures are taken in the G-band filter with the Sun centered in the four quadrants of the 2 k × 2 k CCD (*i.e.*, $[x, y]$ center pixels at approximately $[512, 512]$, $[512, 1536]$, $[1536, 512]$, and $[1536, 1536]$, here 1 pixel $\approx 1.03''$). The combination of the four images serves to fully illuminate the CCD with a fairly featureless disk,

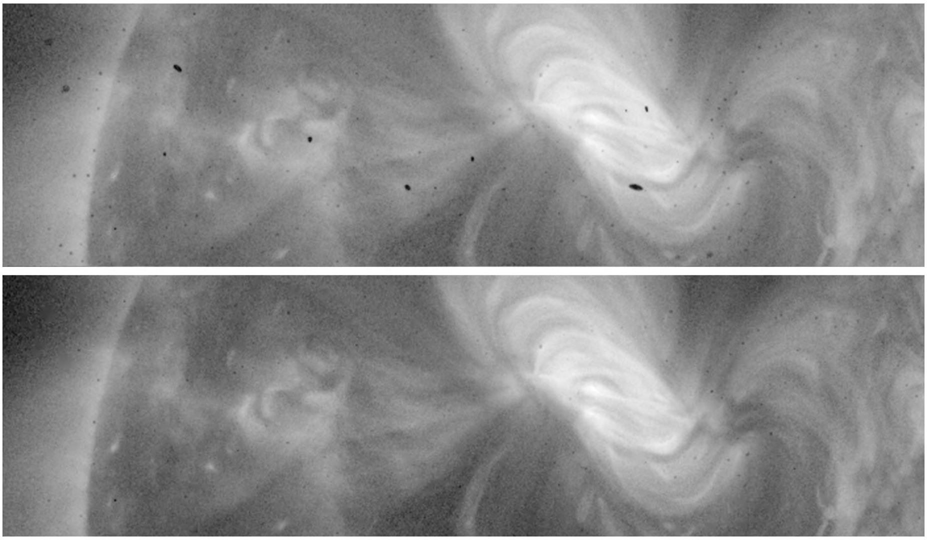

Figure 3 The coronal images before (top) and after (bottom) the spot or dust correction by the SSW procedure, XRT_SPOTCOR. The images are extracted from the observation on 13 June 2013 at 18:05 UT.

and thus make spot or dust identification straightforward. In G-band images, spots appear as bright features, while dusts are small dark features nearly opaque at their centers. In both cases, the features were identified by a relative (fractional) change in intensity exceeding a fixed threshold compared to a heavily smoothed background in fiducial G-band images, with one master spot map per spot epoch, and a single dust map. The use of a relative measurement ensures that spot areas are largely unchanged by changes in the background (which roughly scales with the G-band intensity itself). Spot areas are regularly checked for changes after each CCD bakeout.

The code to perform blemish corrections, XRT_SPOTCOR, is in the SSW tree and is run by XRT_PREP as a part of normal data calibration. Dust and spot maps are read in, the spot and dust features are looped through one by one, and their perimeter pixels are examined. If the blemish data average differs from the boundary pixel average by <2 %, nothing is done. Otherwise, if the feature is large (area >30 pixels) or its boundary flux sufficiently uneven (as gauged by [maximum − minimum]/median value >10 %), the blemish is replaced by using a 2D thin-plate cubic spline from the boundary pixels. If the blemish is small and has a relatively even border, the spot or dust pixels are replaced by a constant value (the median of the boundary pixels). Figure 3 shows coronal images before and after the correction by XRT_SPOTCOR.

There is one additional complication to blemish correction. As noted above, since the entrance filter breach (9 May 2012), the dust specks have varied in size. The added material, however, is only partly opaque and seems to consist of the same material (has similar optical properties) as the contamination layer, although in a more concentrated form. David McKenzie (private communication, 2013) analyzed the area covered by the largest dust feature (centroid at [962, 1120]). He noted that the variation in dust area has a shape similar to the brightness variation at the center of G-band images (see http://xrt.cfa.harvard.edu/missionops/bakeouts/gbandstatus.html), which itself is an indirect measure of the rate of contaminant buildup on the CCD (and filters). This suggests that the dust grains serve as nucleation sites that can attract additional contaminant material after

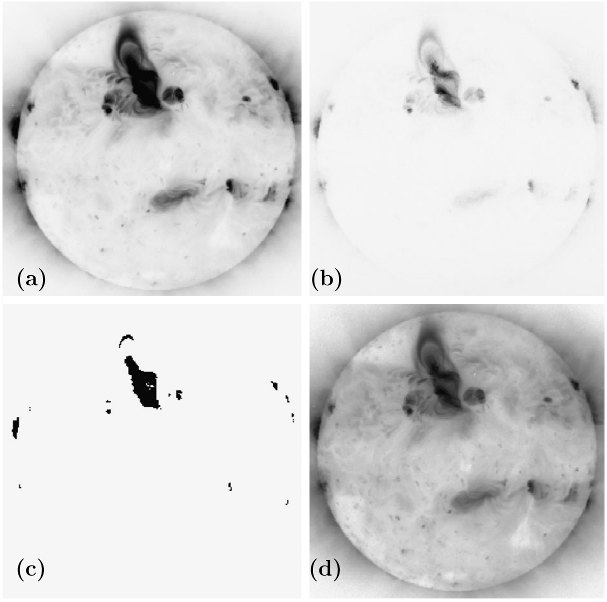

Figure 4 The XRT Ti-poly full-Sun images obtained on 20 January 2012. (a) Image obtained with long exposure (2.05 s). (b) Image with short exposure (0.03 s). (c) A map of saturated pixels of image (a). The black or white areas are to be replaced with the intensities from the long or short exposure images, respectively, to generate a composite image. (d) The resulting composite image made from images (a) and (b).

a bakeout. Somehow the additional light from the light leak acts to fix the newly accreted contaminant to the dust specks. The bakeouts then evaporate a large portion of the accreted contaminant, and the process repeats.

We have taken a smoothed version of McKenzie's dust area values, assumed the growth rate is the same for all dust grains, and found an approximate linear relationship between the dust area, A_{dust}, and the radial extent of the dust growth in pixels (estimated by eye from G-band data): $\Delta r_{\mathrm{dust}} \approx 0.0238 A_{\mathrm{dust}} - 1.019$, where Δr_{dust} is rounded to the nearest pixel. The original dust map is then dilated by Δr_{dust} pixels before blemish correction. The above procedure is performed by `XRT_DUSTGROW`, which is called near the beginning of `XRT_SPOTCOR`, and the dilated dust features are treated as described above. In the future, we will likely try to parameterize the dust growth as a function of G-band brightness or contamination layer thickness, both of which are regularly monitored.

We stress that all of these corrections for dust and spots are purely cosmetic, the corrected pixels will be *approximately* correct, but cannot be trusted as photometric data.

4. Composite Image Preparation

Since the full-Sun images contain a variety of structures with different brightness, it is often difficult to capture all of them properly with a single exposure. Creating a composite image from a few images with different depth of exposures is a simple and convenient method to increase the dynamic range of the intensity. It is performed by replacing the pixels saturated in the longer exposure with those of shorter exposure, as demonstrated in Figure 4. This technique has been commonly used in processing *Yohkoh*/SXT images since the 1990s, although it has not been well explained in publications. In Figure 4 and thereafter the coronal images are shown like negative photographs, *i.e.*, darker pixels have higher intensity, to make faint structures more visible.

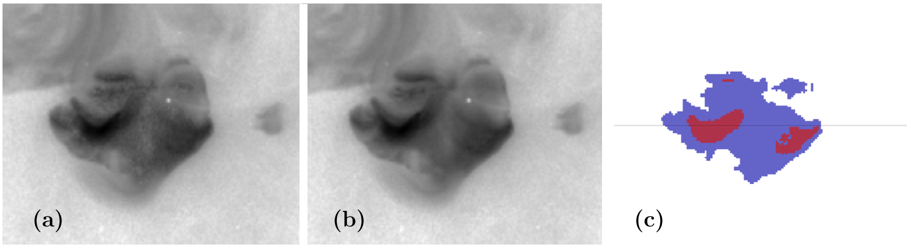

Figure 5 Images of an active region extracted from the full-Sun composite images obtained on 2 June 2013. The composite images are made from (a) the long and short exposures and (b) long, medium, and short exposures. (c) A pixel map showing the contribution to image (b) from the long, medium, and short (white, blue, and red) exposure images, respectively. The black line indicates the location of the intensity profiles shown in Figure 6.

The SCIA images are composite images, except for the images taken with the thick filters (*e.g.*, the thick-Be filter), which have no saturation in most cases. In the initial synoptic programs, the composite images were made from two images, *i.e.* long and short exposures. While the longer exposure time is generally preferred to capture faint structures, the times of the short exposure images are chosen so that the brightest structures do not saturate. Therefore, it is often the case that structures with medium intensity are saturated in the long-exposure image, but do not reach the adequate signal level in the short-exposure image (see Figure 5(a)). Since June 2013, the medium-length exposure was added to the regular synoptic sequences (*e.g.*, the Al-mesh, Ti-poly, and thin-Be filters) to improve the quality of the composite images obtained when solar activity is high and the wide intensity range is required (see Figures 5(b) and (c)). This is confirmed by the intensity profiles shown in Figure 6, in which the medium-exposure image turns out to significantly reduce the noise appearing around 10^4 DN on the two-image composite (compare the blue portion of the intensity profile in the bottom plot with the corresponding portion in the middle plot in Figure 6).

For a quantitative analysis, the errors must be calculated from the original image on which the composite image with the relevant area was based on. While the *Yohkoh*/SXT project provides the uncertainty data array corresponding to each composite image, *Hinode*/XRT provides the software to calculate the uncertainty (`XRT_SYNCOMP_UNC.PRO`).

5. Stray-Light Correction

A sudden increase of intensity was first noted on the visible-light (G-band) images taken on 9 May 2012 and was also recognized as a hazy appearance of daily synoptic images taken from then on with the Ti-poly filter. This problem was very likely caused by the failure of the X-ray pre-filter, *i.e.*, a crack or breach developed probably as a result of thermal stress. A similar situation was experienced by *Yohkoh*/SXT (Acton, 2015), and the same approach for correction turned out to be effective.

5.1. Rationale for the Correction

The visible-light contamination of *Yohkoh*/SXT images was corrected for by the terminator image, which is a stray-light pattern obtained when the satellite is entering or exiting the shadow of the Earth. It uses the window of time when solar X-rays are completely absorbed by Earth's atmosphere before the visible light is starting to fade (see Acton (2015), for details).

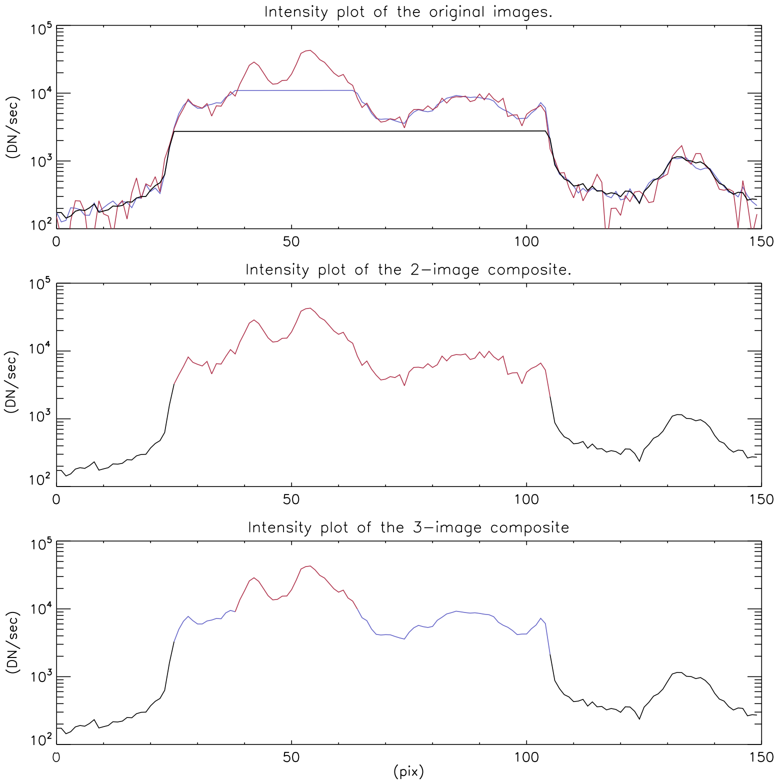

Figure 6 Intensity profiles of the active region along the black line shown in Figure 5(c). Top: Profiles from the long (black), medium (blue), and short (red) exposure images. Middle: Profile of Figure 5(a). Bottom: Profile of Figure 5(b). The black, blue, and red portions indicate the contribution from the long, medium, and short exposure images, respectively.

The same technique is used for the XRT SCIA images considering the different circumstances at data acquisition that mainly result from different orbital elements of the two satellites (see Table 2). Since the *Yohkoh* satellite had a low inclined orbit, the SXT encountered the day-to-night transition in every orbit. This enabled obtaining frequent stray-light correction images. On the other hand, the *Hinode* satellite has a Sun-synchronous polar orbit, so that XRT experiences eclipses only for a few months every year and the depth of the eclipse varies with the phase of the eclipse season. Figure 7 shows the typical light curves observed during *Hinode*'s day-to-night transition in the visible light (with the G-band filter) and X-rays (with the Ti-poly filter). For some time, the X-ray light is completely absorbed by the atmosphere, but the visible light has not yet started to fade. The stray-light pattern to correct X-ray images is obtained in this time window.

5.2. Measurements

A series of studies were performed during the eclipse season of 2014 with the purpose of measuring the amount and spatial distribution of the visible stray light detected through each X-ray filter and its dependence on the satellite pointing (see Table 3). The stray light was measured over the full field of the CCD using 2×2 pixel binning, in accordance with the

Table 2 The circumstances of stray-light image acquisition with *Hinode*/XRT and *Yohkoh*/SXT. The duration of the twilight and the data acquisition window of XRT vary with the depth of the eclipse. See the caption of Figure 7 for additional information.

	XRT	SXT
Orbit (inclination)	Sun synchronous ($\approx$98 deg)	Low inclined ($\approx$31 deg)
Eclipse frequency	$\approx$98 min (as of 2014) early-May to mid-August	$\approx$97 min all year
Duration of twilight	5 to 10 min	Typically 100 s
Data acquisition window	1 to 3 min	Typically 20 s

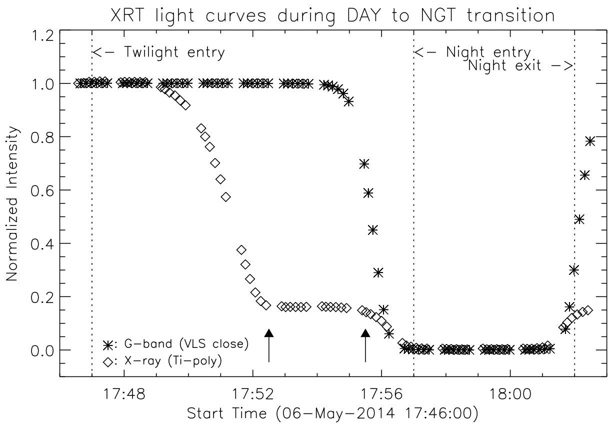

Figure 7 The visible and X-ray light curves obtained during a day-to-night transition of the *Hinode* satellite on 6 May 2014. The asterisks indicate the visible-light (G-band) intensities, while the diamonds show those in the X-ray (Ti-poly). Intensities are normalized with the value of their first images. The timings of twilight entry, night entry, and night exit are provided by *Hinode* ephemeris data, predicted to an accuracy of 30 s. The difference of twilight and night entries defines the duration of the twilight. The plateau appearing in the X-ray light curve between 17:52 to 17:56 UT (two vertical arrows) indicates the visible stray-light component contaminated on the X-ray images.

full-Sun images obtained with the current synoptic observation programs. Each measurement is associated with the acquisition of a few full-Sun images with the same filter as used for the stray-light measurement, and the light curves during the day-to-night transition of the satellite. The latter are obtained by reading out a small region (256 × 256 pixels) near the solar disk center observed in the visible light (G-band filter with visible-light shutter closed) and in the X-rays (Ti-poly filter), both approximately every 10 s (see Figure 7). These measurements are used to confirm that the stray-light pattern was taken at the right timing.

Figure 8 shows the time variation of the Ti-poly filter images obtained during the twilight period of the *Hinode* satellite on 6 May 2014, when the light curves in Figure 7 were observed. In the image obtained at 17:52:40 UT (the left image), the X-ray structures are still observed near the west limb. On the other hand, in the image obtained at 17:55:10 UT (right), the visible light has started to fade from the northeast as the Sun sets toward the southwest direction. Therefore, the image at 17:53 UT (center) has the stray-light pattern that is suitable for correction.

Table 3 Details of the XRT stray-light measurements in the 2014 eclipse season.

Date and time (UT)	Filter (exposure time)	Pointing
6-May-2014, 17:50	Ti-poly (250 ms)	Disk center
15-May-2014, 18:20	Ti-poly (1.4 s), Al-mesh (707 ms)	Disk center
27-May-2014, 20:30	Al-poly (1.0 s), C-poly (1.4 s)	Disk center
3-Jul-2014, 18:30	Ti-poly (1.4 s), Thin-Be (2.8 s)	Disk center
30-Jul-2014, 18:30	Med-Al (32 s)	Disk center
31-Jul-2014, 15:49	Med-Be (24 s)	Disk center
31-Jul-2014, 17:27	Thick-Al (64 s)	Disk center
1-Aug-2014, 16:26	Thick-Be (64 s)	Disk center
8-Aug-2014, 18:56	Ti-poly (4.0 s), C-poly (4.0 s)	North pole
8-Aug-2014, 20:40	Ti-poly (1.4 s), C-poly (1.4 s)	East limb
8-Aug-2014, 22:30	Ti-poly (4.0 s), C-poly (4.0 s)	South pole

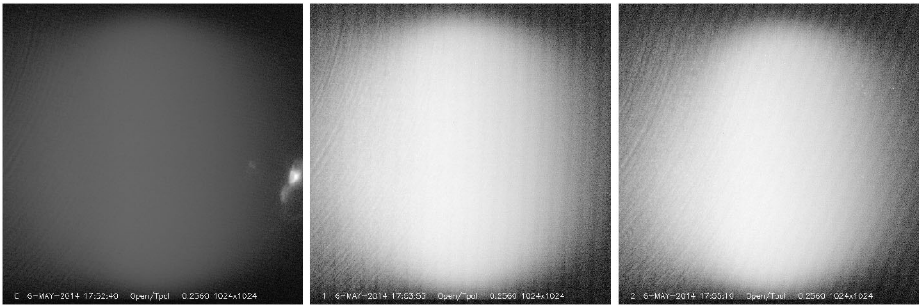

Figure 8 Three consecutive images obtained with the Ti-poly filter during the 6 May 2014 measurement. Pixels with higher intensity are shown brighter here to highlight the faint structures. Left: obtained at 17:52:40 UT. Center: obtained at 17:53:55 UT. Right: obtained at 17:55:10 UT. The center image has the stray-light pattern that is suitable for correction.

5.3. Results

Out of nine X-ray analysis filters measured during the 2014 eclipse season, visible stray light was detected only on the Ti-poly and C-poly filter images, as shown in Figure 9. The observed stray-light pattern appears to have three components. 1) The solar disk component is a blurred image of the solar disk. This is the most dominant component, whose intensity is comparable with the quiet corona. 2) The filter component representes structures peculiar to the filter. It shows wood-grain-like stripes for the Ti-poly and bright wavy streaks for the C-poly filter. The causes of these structures are not understood as yet. 3) The bias component is observed as weak regular stripes that are commonly seen in dark frames of the same size (see Section 2 of Kobelski *et al.*, 2014). This component becomes negligible when the image has sufficiently high signal levels. The intensity profiles of the stray-light images are shown in Figure 10. The profiles are extracted from the horizontal line passing through the center of the image and most substantially represent the solar disk component. The stray light that comes through the Ti-poly filter is roughly three times more intense than the one that comes through the C-poly filter and is weaker than $1/1000$ of the visible stray light observed through the G-band filter.

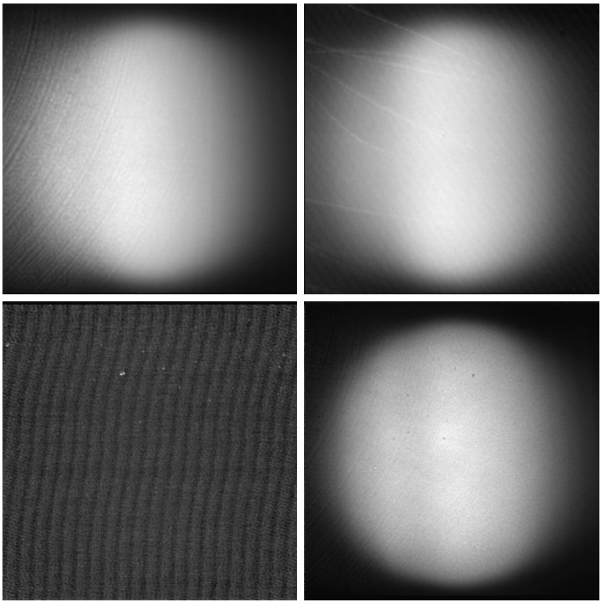

Figure 9 Stray-light patterns measured at the disk center pointing. Top left: Ti-poly filter obtained at 18:25:03 UT on 15 May 2014. Top right: C-poly filter at 20:46:01 UT on 27 May 2014. Bottom left: Al-mesh filter at 18:25:11 UT on 15 May 2014. The CCD bias component (see text) alone is observed. Bottom right: G-band filter (with the visible-light shutter closed) at 18:04:37 UT on 15 May 2014, showing that the solar disk component (see text) is dominant and has a higher contrast than in the X-ray filters. Brighter pixels indicate higher intensity.

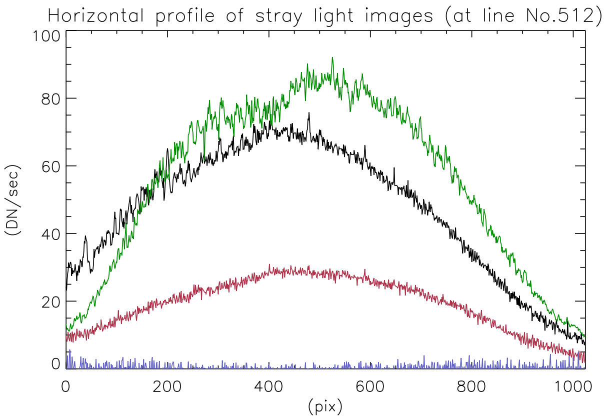

Figure 10 Intensity profiles of the stray light images shown in Figure 9 measured with the Ti-poly (black), C-poly (red), Al-mesh (blue), and G-band (green) filters. Note that the G-band stray light intensity is divided by 1200 to fit in the same scale range as the X-ray filters. The profiles are along the horizontal line passing through the image center, *i.e.* at the line No. 512. Intensities have had the dark bias subtracted.

As the images in Figure 11 show, the solar disk component of the stray-light patterns is significantly affected by the satellite pointing. This indicates that the coronal images must be corrected for by the stray-light pattern obtained under the same pointing condition, which poses the challenge of correcting the partial-Sun images acquired at the various pointing locations. It is interesting to note that the filter component on C-poly images varies significantly with pointing, while that on Ti-poly images appears to be steady.

Figure 12 shows that the Ti-poly and C-poly coronal images are successfully corrected for by the stray-light images obtained closely in time with the same filter under the same pointing condition. In both cases, the faint coronal structures, such as coronal hole boundaries, are more visible, and the filter-component of the stray-light patterns is entirely corrected (see Figure 13 for details). The contaminated coronal images with the Ti-poly and C-poly X-ray analysis filters are well corrected by the visible stray-light patterns obtained using the satellite eclipses. This shows that the additional intensity contamination of the

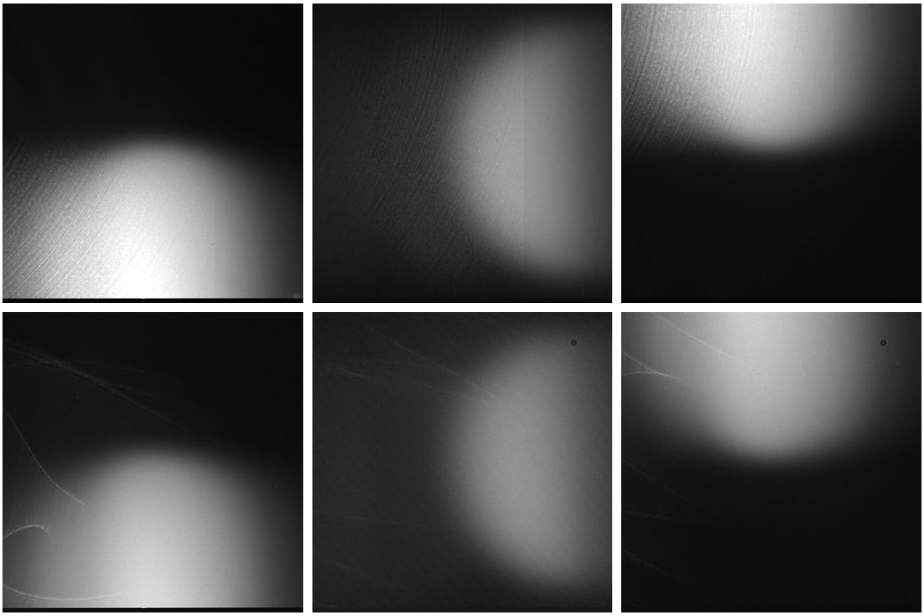

Figure 11 Stray-light patterns measured under different conditions of satellite pointing on 8 August 2014. The top and bottom images are obtained with the Ti-poly and C-poly filters, respectively. Left: North pole pointing obtained at 19:11:24 UT/19:11:37 UT. Center: East limb pointing at 20:50:20 UT/20:50:30 UT. Right: South pole pointing at 22:29:05 UT/22:29:18 UT.

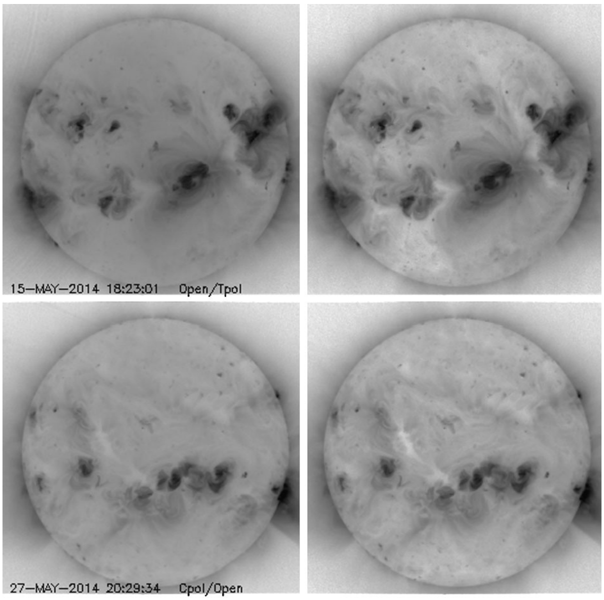

Figure 12 Top: Ti-poly composite full-Sun images on 15 May 2014, 18:23 UT. Before (left) and after (right) subtracting the stray-light image shown in Figure 9. Bottom: C-poly coronal images on 27 May 2014, 20:29 UT. Before (left) and after (right) stray-light subtraction.

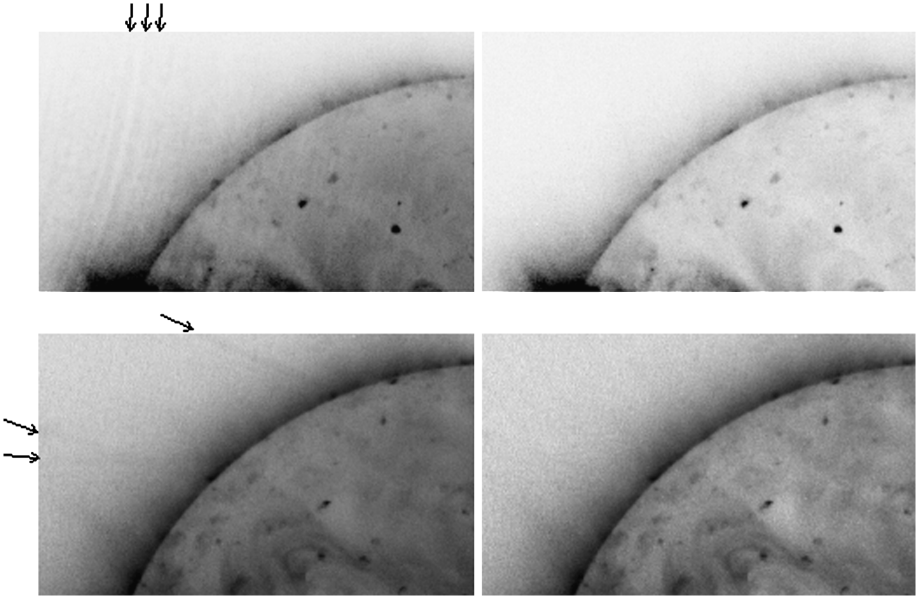

Figure 13 The close-up of images in Figure 12 of the area of the northeast limb. The filter component of the stray light is remarkably clear in the left images (examples are shown with arrows), while these structures are entirely invisible in the right images. The top and bottom images are obtained with the Ti-poly and C-poly filter, respectively.

X-ray signals is caused by visible-light leakage into the X-ray telescope and is detected through the Ti-poly and C-poly X-ray filters.

The signals corrected for by the above method are quantitatively reliable when the stray-light image was obtained under the same conditions (*e.g.*, time, filter, and pointing) as the coronal images to be corrected. However, since the stray-light images are only acquired through the use of *Hinode*'s eclipses, most of the images do not have the exact stray-light pattern usable for correction. For this reason, the stray-light correction is not applied for the SCIA FITS files or the quantitative treatment of the signals. Assuming and subtracting the reasonable amount of stray-light component requires case-by-case treatment and thus is left to individual users. In contrast, the stray-light correction is applied to the browse images (in PNG format) from 9 May 2012 to the present. The stray-light intensities for correcting the images obtained outside the 2014 eclipse season were estimated by the method described in the following sections.

5.4. Temporal Variation of the Stray-Light Intensity

The two Ti-poly stray-light images measured more than one month apart in 2014 (*cf.* Table 3) show that there was no substantial change detected between them in the observed patterns. Their residual intensity was lower than $\pm 5\ \mathrm{DN\,s^{-1}}$ over the whole area. Therefore, the stray-light pattern of 15 May 2014 is usable for correcting the coronal images taken in July 2014. However, the same stray-light image turned out to overcorrect the coronal images of May 2012, indicating that the stray-light intensity has increased in two years. Given the fact that the stray-light images are only obtained during the eclipse seasons, it is crucial to know the temporal variation of the stray-light intensity to correct the coronal images outside eclipse seasons.

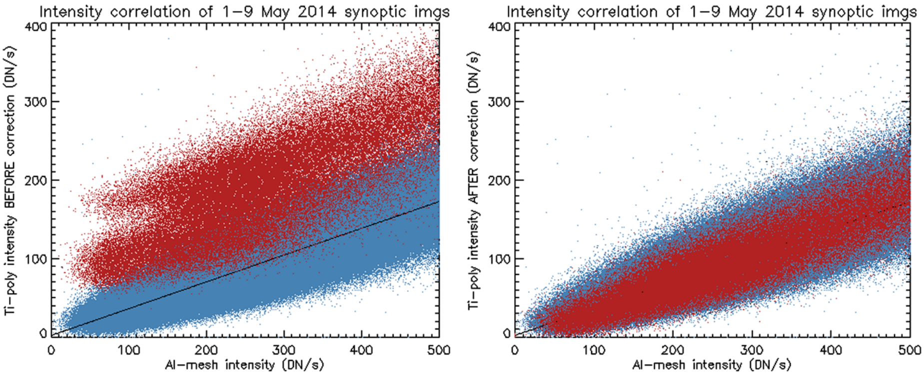

Figure 14 Cross correlation of the Al-mesh and Ti-poly intensities obtained on 1 to 9 May 2012. The data points before and after the stray-light problem occurred are shown with blue and red dots, respectively. The Ti-poly image is uncorrected in the left plot, while it is corrected in the right plot by subtracting the stray-light image obtained in 2014, multiplied by 0.5. The black line in the left plot is the linear regression of the blue data points. See the text for details.

Two scatter plots in Figure 14 show the intensity correlations between the coronal images taken with the Al-mesh filter and the Ti-poly filter. We note that the former images are free from the visible stray light, and each filter pair was obtained in the same synoptic program, *i.e.*, their acquisition times differ by less than one minute. The plots are made of the pixels of on-disk quiet regions within 0.9 $R_\odot$, as they have comparable intensities with the stray light on the Ti-poly filter images. The red dots are the data points from the first pair of images after the stray light was noticed (9 May 2012, 18:03 UT), while the blue dots indicate those from 17 pairs of images obtained in May 2012, before the incidence of the stray-light problem. The left plot shows the deviation of the red data points from the previous trend (blue data points) caused by the stray-light contamination. The right plot shows that the correction of the Ti-poly intensities in the form of the following equation is successful,

$$I_{\mathrm{corr}} = I_{\mathrm{uncor}} - k * I_{\mathrm{sl}}, \tag{1}$$

where I_{corr} and I_{uncor} are the intensities of the Ti-poly image after and before correction, respectively. I_{sl} is the intensity of the stray-light image obtained on 15 May 2014. The scalar factor, k, is determined so that the data points of the corrected image minimize the square sum of the difference from the linear regression line of the data points before the stray-light problem (the black line in Figure 14). It is chosen to be 0.5 in this case.

Figure 15 shows the value of k, determined for the pairs of Al-mesh and Ti-poly images available from 9 May 2012 through 31 December 2014. As a general trend, the stray-light intensity tends to gradually increase and reach the current level at the beginning of 2013. A series of short increments of roughly three weeks appears to reflect the increase of visible-light intensity as a result of the building-up of the contaminants on the CCD, and their clearance by the CCD bakeout operations. Narukage *et al.* (2011) reported that the layer of the CCD contaminants enhances the visible-light intensity because the layer attenuates the reflection from the CCD surface and relatively enhances the transmission. For simplicity, the smoothed values of k, shown as the blue line in Figure 15, were used to correct the T-poly and C-poly browse images (PNG format) in the SCIA. This is obtained by shifting the line of a seventh-order polynomial fit to the data points (red line) downward by 0.05. The lower envelope of the data points was chosen to avoid overcorrected intensities from becoming negative.

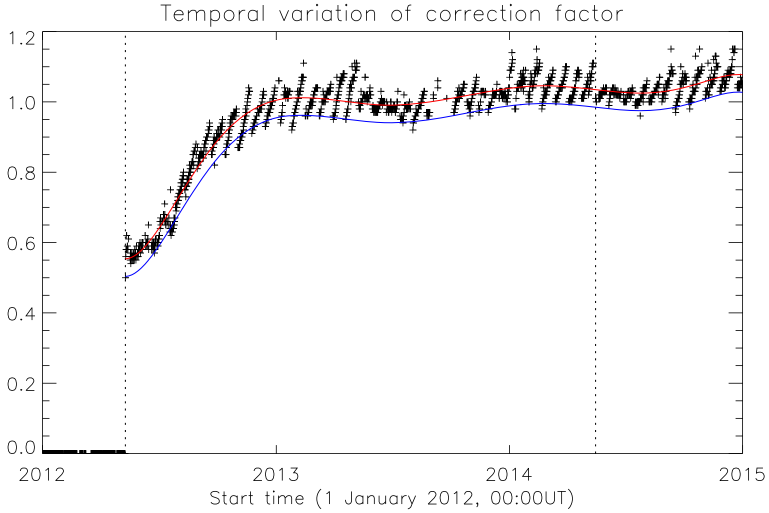

Figure 15 Temporal variation of the factor, k, determined from the correction of Ti-poly images through Equation (1). The vertical lines indicate two notable events: 9 May 2012, when the pre-filter failure occurred, and 15 May 2014, 18:25 UT, when the Ti-poly stray-light image used for this analysis was obtained. The red line is the polynomial fit to the data points. The blue line represents the practical values of the correction factor applied to the SCIA browse images, obtained by shifting down the polynomial fit by the amount 0.05.

In contrast, this correction was not applied to the corresponding FITS products in the SCIA. More precise values of stray light should be used for quantitative studies. The k values in Figure 15 are only available for the Ti-poly images that have an Al-mesh image to pair it with, and each of the paired images includes no bad pixels, such as saturation or telemetry dropouts. For other images, the amount of stray light should be estimated by, for example, interpolating the data points for the short period of time between the two successive CCD bakeout operations. This type of detailed correction for all Ti-poly and C-poly contaminated images is still under consideration and is not yet included in the current official FITS products.

6. Conclusions

The XRT synoptic composite image archive was developed to provide the soft X-ray full-Sun images obtained with *Hinode*/XRT since November 2006. The following techniques are used to improve the quality of the archived images.

1) The small dark spots resulting from the contaminants agglomerated on the CCD are removed by replacing the spots with the averaged intensity of the surrounding area. 2) The full-Sun images of a given X-ray analysis filter are obtained with two or three different exposure times and are processed to composite images to increase the intensity dynamic range as a whole. 3) The visible stray-light contamination on T-poly and C-poly filter images resulting from the X-ray pre-filter failure is corrected for by the stray-light pattern obtained during the eclipse season of the *Hinode* satellite. No visible-light component was detected in the other X-ray filter images. 4) The pointing information is updated by the recently developed co-alignment database.

Two types of images are available to the public from the web site, http://solar.physics.montana.edu/hinode/xrt/. The PNG images are spot-corrected, composite, stray-light subtracted, and their intensities are arbitrarily scaled for best viewing. The FITS images are simply spot-corrected and composite, so that users can apply quantitative analyses.

Additional note: On 14 June 2015, while revising this manuscript, XRT experienced another increase of visible stray light. The new method of calibration is under investigation.

Acknowledgements *Hinode* is a Japanese mission developed and launched by ISAS/JAXA, with NAOJ as domestic partner and NASA and STFC (UK) as international partners. It is operated by these agencies in co-operation with ESA and the NSC (Norway). This work was supported by NASA grant NNM07AB07C for *Hinode* XRT science. We thank David McKenzie for providing the dust size measurements. We also thank Patrick MacCauley, Adam Kobelski, and Nicole Schanche for their help in characterizing the effects of the light leak, and we thank Antonia Savcheva and Patricia Jibben for the help in developing and testing the spot-correction code. AT thanks Loren Acton for helpful comments and wording advice.

References

Acton, L.W.: 2015, On-orbit performance and calibration of the Soft X-ray Telescope on Yohkoh. *Solar Phys.*, in press.

Freeland, S.L., Handy, B.N.: 1998, Data analysis with the SolarSoft system. *Solar Phys.* **182**, 497. ADS.

Golub, L., Deluca, E., Austin, G., Bookbinder, J., Caldwell, D., Cheimets, P., Cirtain, J., Cosmo, M., Reid, P., Sette, A., Weber, M., Sakao, T., Kano, R., Shibasaki, K., Hara, H., Tsuneta, S., Kumagai, K., Tamura, T., Shimojo, M., McCracken, J., Carpenter, J., Haight, H., Siler, R., Wright, E., Tucker, J., Rutledge, H., Barbera, M., Peres, G., Varisco, S.: 2007, The X-Ray Telescope (XRT) for the *Hinode* mission. *Solar Phys.* **243**, 63. DOI. ADS.

Kobelski, A.R., Saar, S.H., Weber, M.A., McKenzie, D.E., Reeves, K.K.: 2014, Calibrating data from the *Hinode*/X-Ray Telescope and associated uncertainties. *Solar Phys.* **289**, 2781. DOI. ADS.

Kosugi, T., Matsuzaki, K., Sakao, T., Shimizu, T., Sone, Y., Tachikawa, S., Hashimoto, T., Minesugi, K., Ohnishi, A., Yamada, T., Tsuneta, S., Hara, H., Ichimoto, K., Suematsu, Y., Shimojo, M., Watanabe, T., Shimada, S., Davis, J.M., Hill, L.D., Owens, J.K., Title, A.M., Culhane, J.L., Harra, L.K., Doschek, G.A., Golub, L.: 2007, The *Hinode* (Solar-B) mission: An overview. *Solar Phys.* **243**, 3. DOI. ADS.

Narukage, N., Sakao, T., Kano, R., Hara, H., Shimojo, M., Bando, T., Urayama, F., Deluca, E., Golub, L., Weber, M., Grigis, P., Cirtain, J., Tsuneta, S.: 2011, Coronal-temperature-diagnostic capability of the *Hinode*/X-Ray Telescope based on self-consistent calibration. *Solar Phys.* **269**, 169. DOI. ADS.

Narukage, N., Sakao, T., Kano, R., Shimojo, M., Winebarger, A., Weber, M., Reeves, K.K.: 2014, Coronal-temperature-diagnostic capability of the *Hinode*/X-Ray Telescope based on self-consistent calibration. II. Calibration with on-orbit data. *Solar Phys.* **289**, 1029. DOI. ADS.

Ogawara, Y., Takano, T., Kato, T., Kosugi, T., Tsuneta, S., Watanabe, T., Kondo, I., Uchida, Y.: 1991, The Solar-A mission – An overview. *Solar Phys.* **136**, 1. DOI. ADS.

Tsuneta, S., Acton, L., Bruner, M., Lemen, J., Brown, W., Caravalho, R., Catura, R., Freeland, S., Jurcevich, B., Morrison, M., Ogawara, Y., Hirayama, T., Owens, J.: 1991, The Soft X-ray Telescope for the SOLAR-A mission. *Solar Phys.* **136**, 37. DOI. ADS.

Yoshimura, K., McKenzie, D.E.: 2015, Calibration of *Hinode*/XRT for coalignment. *Solar Phys.* **290**, 2355. DOI. ADS.